Supplementary Information: Monolithic Integration of Piezo-Optomechanical Photonics and CMOS Electronics

Matthew Zimmermann[1,†], Aileen Zhai[2], Andrew J. Leenheer[3], Julia Boyle[1], Mayank Mishra[4], Daniel Dominguez[3], Matt Koppa[3], Wolf Jehle[3], Christopher Panuski[5], Mark Dong[1,5], Gerald Gilbert[6], Dirk Englund[5], and Matt Eichenfield[2,3,4,&]

[1]*The MITRE Corporation, 202 Burlington Road, Bedford, Massachusetts 01730, USA*
[2]*Electrical, Computer, and Energy Engineering, University of Colorado Boulder, Boulder, Colorado 80309, USA*
[3]*Sandia National Laboratories, P.O. Box 5800 Albuquerque, New Mexico 87185, USA*
[4]*Wyant College of Optical Sciences, University of Arizona, Tucson, Arizona 85719, USA*
[5]*Research Laboratory of Electronics, Massachusetts Institute of Technology, Cambridge, Massachusetts 02139, USA*
[6]*The MITRE Corporation, 200 Forrestal Road, Princeton, New Jersey 08540, USA*
[†] mzimmermann@mitre.org, [&] matt.eichenfield@colorado.edu

Table of Contents

Table of Contents
SI-1. Electronic Backplane Wafer Information and Processing
SI-2. Wafer-scale Photonic and Electronic Characterization
SI-3. Die-Level Active Backplane Measurement and Data Processing
SI-4. Power and Thermal Analysis
SI-5. Wafer-Scale Autoprober Measurement and Analysis of EIC-PIC
SI-6. H-CMZI Data Analysis
SI-7. MZI Modeling and Fitting to Experimental Data
SI-8. Ring Resonator Modeling and Analysis
Supplementary References

SI-1. Electronic Backplane Wafer Information and Processing

The electronic backplane was a commercially-available 200mm CMOS wafer designed for MicroLED displays (JD2552 microdisplay die) from Jasper Display Corporation, fabricated with a 45 nm process from a Fujitsu foundry. Each reticle contained logic to route a proprietary high-speed parallel data protocol from a flex ribbon cable to voltages on the pixel backplane in the center of the chip. The high speed data signal is driven from the JD30U1 OCM Controller Driver Board, which converts a 1920x1080, 60 Hz HDMI image to signals which route high speed data, control, power, and clock signals over a Flexible PCB interposer. The interposer contains multiple rows of bond pads that wirebond to 121 pads on the edge of the die. The electronic backplane contained an array of pixels in the center of the die in a HD display

configuration of 1920 columns and 1080 rows, and individual pixels had a pitch of 6.4 um. The backplane controlled each pixel with a pulse-width modulated digital signal ranging from 0-5V with variable duty cycle based on desired pixel intensity.

Each wafer has a thin passivation layer with a stack of one silicon dioxide (SiO2) and one Silicon Nitride (Si3N4) layers, with total thickness of approximately 150 nm. To monolithically integrate our piezo-optomechanical photonic integrated circuit and connect it directly to the metal in the pixel backplane, we first prepare the wafer by microdrilling holes through the passivation layer with a laser. These microdrilled holes allow us a direct electrical connection to both the electronic signals in the pixel backplane and to the control bond pads at the edge of the chip. After microdrilling holes, we begin PIC fabrication using the process outlined in prior work[1] [2]. Alignment of the first metal layer with the underlying electronic integrated circuit was critical in matching the PIC devices to the pixel backplane; manual adjustment and optical alignment to features on chip was done to ensure the lithography was aligned well enough to perfectly align reticles to the pixel backplane. After wafer fabrication, individual die are diced and undergo a release process of Xenon Diflouride (XeF_2) to release the MEMS devices and enhance their actuation. All PIC fabrication was done at Sandia National Laboratories.

SI-2. Wafer-scale Photonic and Electronic Characterization

We measure the passive photonic behavior and basic electronic behavior of devices across a wafer using an automated electronic and photonic probe station (MPI 2000) at Sandia National Laboratories. We verify the backplane electronics by measuring electrical connectivity between control pads on shared electronic planes, and by measuring high impedance between pads on different electronic planes. This gives us confidence that the exposed bond pads at the top of the photonic integrated circuit connect to the underlying CMOS logic of the electronic integrated circuit.

Using a fiber array for photonic autoprobing, we verify passive photonic performance of the SMZI tree, V-CMZI devices, and optical ring resonators. We also sweep our optical ring resonators with a tunable laser to measure the quality factor of thousands of rings across the wafer. We measure the loaded quality factor by fitting a lorenzian curve to our wavelength sweeps, measuring the full width half maximum spectral width $\Delta\lambda$ by a resonant dip, and calculating $Q=\lambda_0/\Delta\lambda$. We measure loaded Q factors up to 2×10^4 in annular rings and up to 7×10^5 in pie wedge rings from wafer-scale autoprobing, and find consistently high quality factors when using a thru-port waveguide width of 400 nm, a ring waveguide width of 300 nm, and a coupling gap between 200nm-260 nm.

SI-3. Die-Level Active Backplane Measurement and Data Processing

Experimental testing using an active backplane was done at the MITRE corporation. Three die from different locations on the wafer were diced, released with a XeF_2 gas, and wirebonded to vendor-supplied Flexible Interposer Printed Circuit Boards. The interposer PCB is connected to the driver board, which converts a 1920x1080 image coming from a PC into the high speed signals to program the chip. Custom python software was developed to generate arbitrary images which map pixels to actuatable segments on a chip.

The driver board and PIC-on-EIC die are placed under a microscope, and coherent light from a tunable laser (Sacher Lasertechnik X500-0730-010, 720-740 nm tuning range and Sacher Lasertechnik X500-0780-030, 770-810 nm tuning range) was sent through single mode fiber through a 3-paddle manual polarizer and a multi-port fiber array was used to couple light into and out of optical gratings on the PIC. Gatings were designed for TE polarization, and we set polarization by maximizing the power through the chip. We also use an electronic probe to measure an ‘alignment pixel’ we have routed to an exposed top metal pad, so we can monitor the driving signal from the backplane and verify it is producing a 5V Pulse Width Modulated pattern that is synchronized with our PIC device modulation.

The PIC output was measured from two ports on the fiber array connected to two fiber coupled high speed photodiodes (Newport 1801-FC) with a bandwidth from DC-125 MHz. Raw power levels from photodiodes and the alignment pixel were recorded using a Multifunction Test Instrument (Liquid Instruments Moku:Pro) capable of high-speed signal measurement via electronic oscilloscope and electronic data logger toolboxes. The data logger toolbox was used to measure the optical output powers while sweeping a laser at a constant rate or while modulating the pixel backplane. Because the pixel backplane produced a flickering digital signal based on the HDMI, the high-speed data was analyzed to record the photodiode voltage of where the settled signal was. This process is shown in Fig. SI-1. Photodiode measurements were then scaled, normalized, and converted to estimated phase shift.

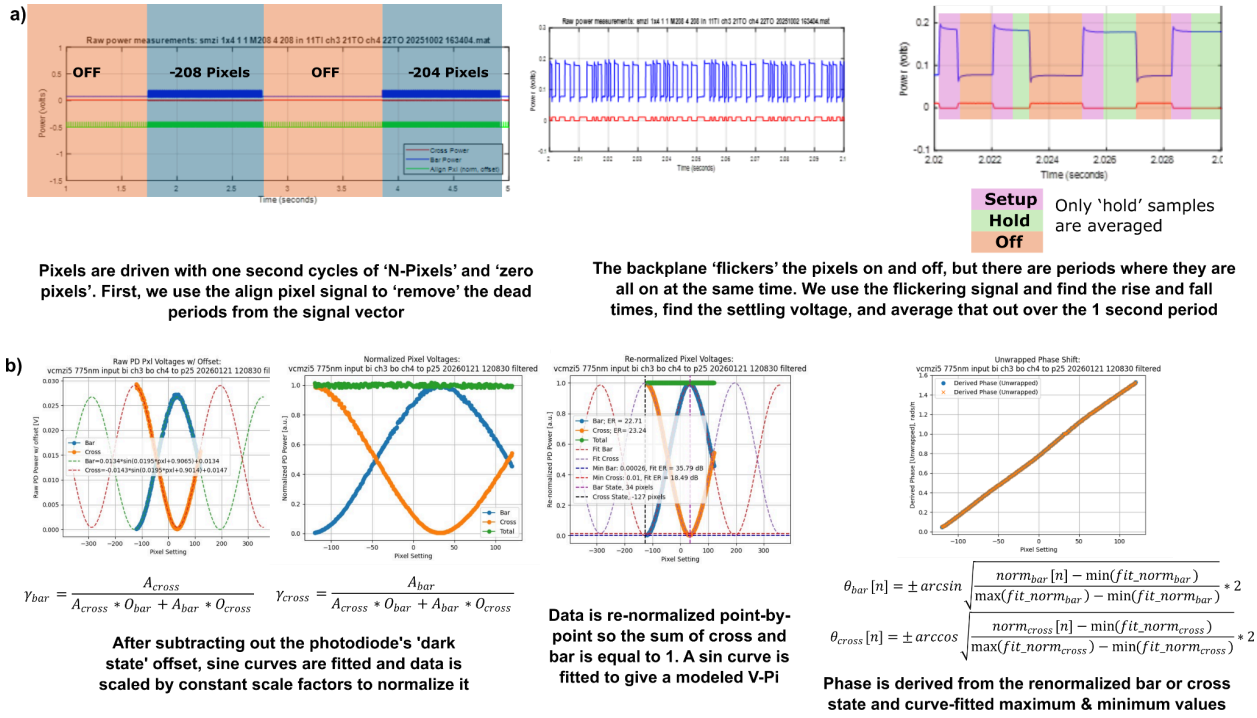

Fig. SI-1 | Experimental Measurement and Data Processing. a, Data from the high-speed photodiodes and an electronic driving pixel is logged over the course of several seconds while modulating various segments on the backplane. This data is analyzed and the 'settled' state is extracted. **b,** From the raw settled photodiode value, we can extract the normalized bar and cross states and the derived phase. A fitted sinusoidal curve shows us the expected extinction beyond the tuning range of our device.

SI-4. Power and Thermal Analysis

Capacitances are calculated using the parallel plate capacitance equation $C = \frac{A\epsilon_0\epsilon_R}{d}$, where A is the area of the overlapping metal layers, $\epsilon_0 = 8.85e - 12$ (permittivity of free space), $\epsilon_R = 9$ (permittivity of Aluminum Nitride), and d=450 nm (depth of the aluminum nitride layer).

The backplane temperature was monitored with an FLIR thermal camera. With no active cooling, we observed a temperature of 24° C (room temperature) when the system was powered down, 27° C when the system was on and no pixels were driven, and 32.6° C when the system was on and all pixels were driven, for a temperature change of approximately 7.6° C between being completely off (room temperature) and being on with all pixels and photonics being driven.

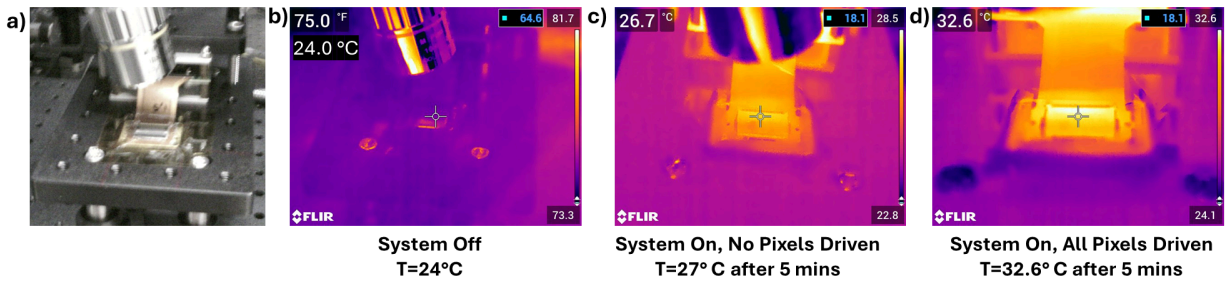

Fig. SI-2 | Thermal measurements of EIC-PIC a) Full color photograph of test setup. b) FLIR image of chip with system off. c) FLIR image of chip with no pixels driven, after running system for 5 minutes. d) FLIR image of system with all pixels driven, after running for 5 minutes. (T=32.6)

SI-5. Wafer-Scale Autoprober Measurement and Analysis of EIC-PIC

Data Acquisition on the Whole Wafer Using the Autoprober Platform

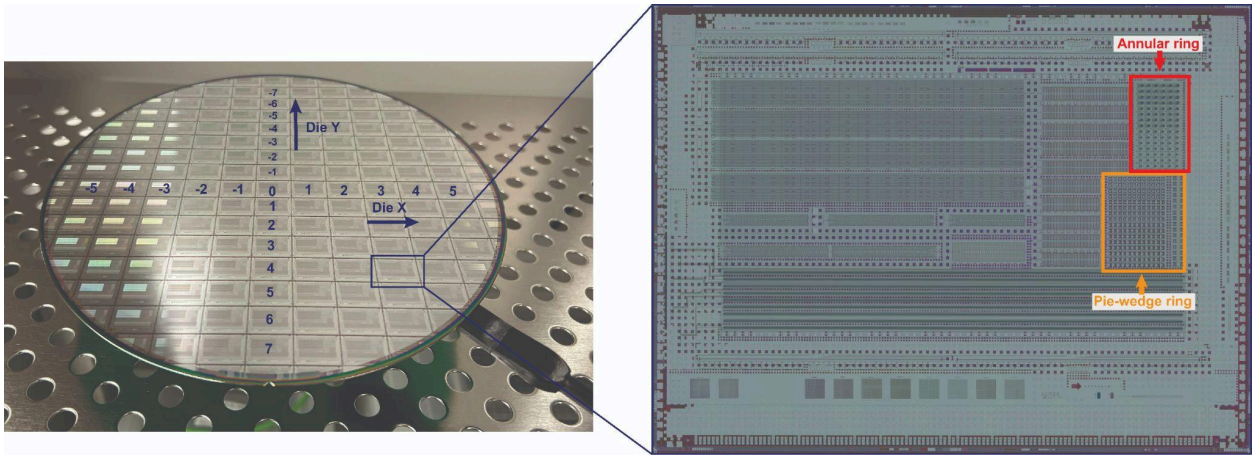

Fig. SI-3 | Data Acquisition on the Whole Wafer Using the Autoprober Platform a) Wafer image of the platform showing the marked dies, with the DieX and DieY axes indicating the wafer coordinates used in the automated annular and pie-wedge ring resonator data acquisition. b) Optical micrograph of a die, highlighting the pie-wedge ring resonators (orange) and annular ring resonators (red) used for the Q-factor measurements.

For these measurements, the autoprober platform used three voltage channels of an NI-6216 DAQ sampled at 1 kHz to acquire all optical and control signals synchronously. Channel 0 recorded the transmission from output 1 using a Thorlabs DET02AFC detector (responsivity approximately 0.46 A/W) followed by an SR570 transimpedance amplifier set to 5 MΩ/A, which converted the optical power at the measured port into a voltage compatible with the DAQ. Channel 1 recorded the laser controller $V(\lambda) = \frac{\lambda_{act} - \lambda_{min}}{\lambda_{max} - \lambda_{min}}$ V output during the wavelength sweep from 765 nm to 781 nm at 4 nm/s, providing the calibration needed to map time, and therefore all

simultaneously acquired channels, to instantaneous wavelength and to reconstruct transmission-versus-wavelength traces. Channel 2 monitored a second output using a PM101A with an S150C sensor; its analog output (7.5 kV/W) was amplified by an SR560 set to a gain of 2000 before digitization to compensate for the lower signal level on that port. This acquisition scheme kept all channels time-aligned, while the linear region of Channel 1 defined the usable wavelength window for connectivity checks and transmission analysis.

For annular ring resonators, this procedure was repeated across 14 distinct die locations on the wafer, corresponding to combinations of DieX = −3, 0, and 3 and DieY = 3, 2, 0, −2, −3, and −5. Each die contained 96 test sites (Site1–Site96), with systematically varied bus-waveguide width (0.35 µm, 0.4 µm), ring-waveguide width (0.3 µm, 0.35 µm, 0.4 µm), ring-to-bus gap (0.2 µm, 0.21 µm, 0.22 µm, 0.24 µm), and ring radius (10 µm, 15 µm, 25 µm, 30 µm) to enable statistical sampling of device performance across the wafer field.

For pie-wedge ring resonators, this procedure was repeated across 29 distinct die locations on the wafer, spanning combinations of DieX from −5 to 4 and DieY from −1 to 3; each die contained 192 test sites (Site1–Site192) [file:65]. Within each die, the design systematically varied the bus-waveguide width (0.3 µm, 0.35 µm, 0.4 µm), ring-waveguide width (0.25 µm, 0.3 µm, 0.35 µm, 0.4 µm), ring-to-bus gap (0.2 µm, 0.21 µm, 0.22 µm, 0.24 µm), and ring radius (15 µm, 20 µm, 30 µm, 40 µm) to enable statistical sampling of device performance across the wafer field.

Data analysis of the annular ring resonators and pie-wedge ring resonators

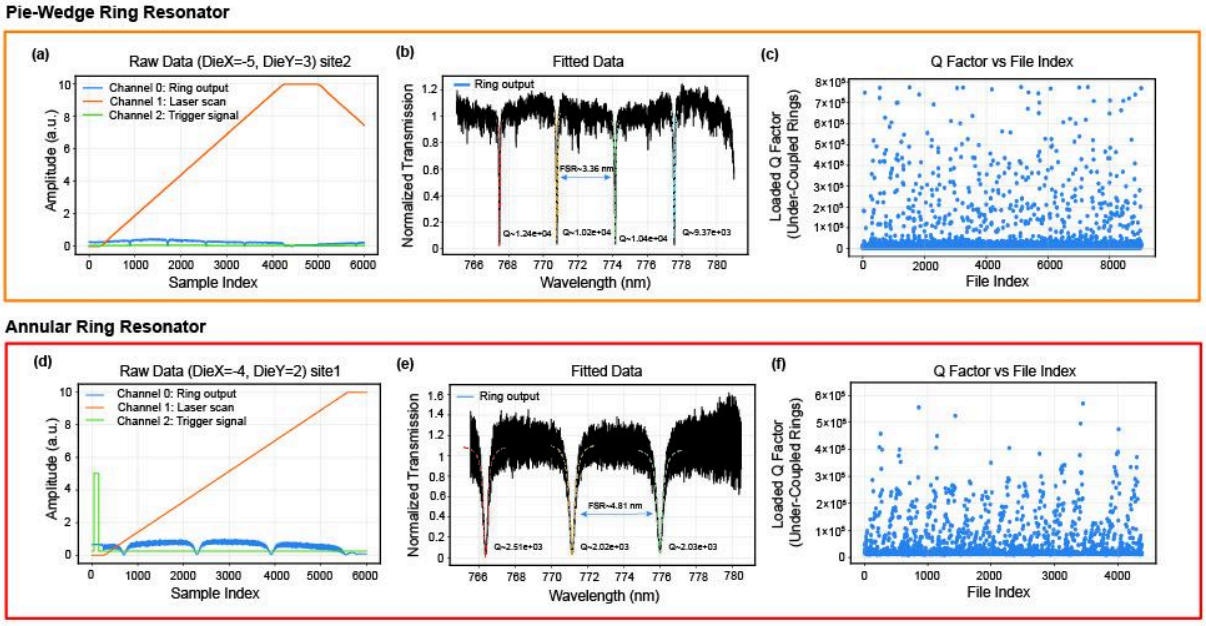

Fig. SI-4 | Resonator transmission and Q-factor statistics across the wafer. a) Autoprober raw transmission data for a pie-wedge ring, showing the three simultaneously recorded channels used in the analysis. b) Normalized transmission spectrum (Channel 0) and Lorentzian fit for a pie-wedge ring at (DieX, DieY) = (−5, 3), Site 2, used to extract the loaded quality factor. c) Loaded Q factors for all pie-wedge rings measured across the wafer, highlighting uniform performance. d) Autoprober raw transmission data for an annular ring, showing the same three measurement channels. e) Normalized transmission spectrum and Lorentzian fit for an annular ring at (DieX, DieY) = (−4, 2), Site 1. f) Loaded Q factors for all annular rings measured across the wafer.

We analyzed the wavelength-swept transmission traces recorded with the autoprober to extract key resonance parameters for both the annular and pie-wedge ring resonators. Figure 2(a,d) shows representative raw data from two rings. We normalized each spectrum, as illustrated in Fig. 2(b,e), to correct for laser power drift and wavelength-dependent variations in fiber-to-chip coupling across the Channel 1 sweep window. An automated fitting routine identified the resonance minima and locally fitted each feature with either a Lorentzian profile (for under-coupled and critically coupled resonances) or a Fano-type profile (for asymmetric responses). These fits yielded the resonance wavelength, loaded quality factor, and free-spectral range of each ring.

For the pie-wedge rings, we performed this analysis on 192 sites across each of the 29 dies, enabling a multidimensional assessment of how wedge geometry, coupling gap, and ring radius influence intrinsic loss. These devices consistently exhibited loaded quality factors in the few-10^5 range, as summarized in Fig. 2(c). For the annular rings, we analyzed data from 96 sites on each of the 14 dies to identify trends in quality factor and free-spectral range with respect to bus-waveguide width, ring-waveguide width, ring-to-bus gap, and ring radius. As shown in Fig. 2(f), the annular rings exhibited loaded quality factors on the order of 10^4. For both ring types, increasing the coupling gap shifted the devices further into the under-coupled regime, and the intrinsic quality factors remained comparable to the loaded values.

SI-6. H-CMZI Data Analysis

Because the Horizontal CMZI had a non-linear response due to its unique design, we analyse the device in two ways. First, we sweep the number of active segments from the maximum negative to maximum positive settings, derive the phase shift, and take the difference to find the phase shift per segment. We also perform a ‘One-Hot’ phase sweep, where we only set one segment active at a time and measure the phase shift each active segment imparts in isolation. We note the segments in Fig. SI-5a as $\theta_{ARM,GROUP}$, where ‘ARM’ is 1 (top) or 2 (bottom) and ‘GROUP’ ranges from 1 (outermost arm) to 8 (innermost arm).

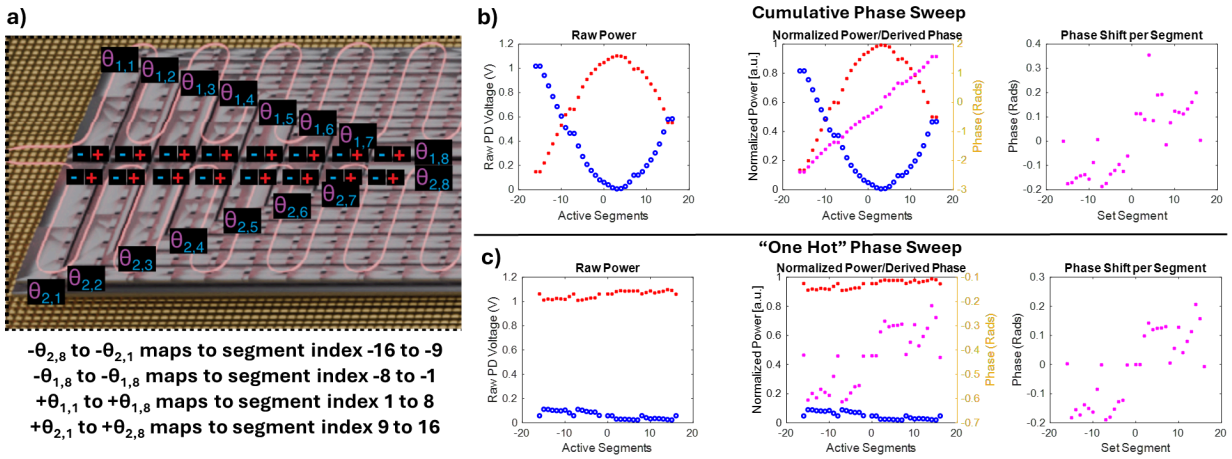

d)

	Difference from Phase Sweep					One-Hot Test					
Segment group	Top M3 (+)	Top M2 (-)	Bottom M2 (+)	Bottom M3 (-)	Mean	Top M3 (+)	Top M2 (-)	Bottom M2 (+)	Bottom M3 (-)	Mean	Mean Sweep-OneHot
1	0.082	0.071		0.069	0.074	0.069		0.061	0.070	0.066	0.008
2	0.130	0.093		0.123	0.115	0.122	0.101	0.101	0.122	0.111	0.004
3	0.114	0.104	0.136	0.114	0.117	0.114	0.084	0.082	0.107	0.097	0.020
4	0.116	0.089	0.078	0.107	0.098	0.117	0.085	0.091	0.114	0.102	-0.004
5	0.121	0.105	0.108	0.126	0.115	0.130	0.111	0.104	0.123	0.117	-0.002
6	0.167	0.147	0.104	0.135	0.138	0.146	0.129	0.132	0.139	0.136	0.002
7		0.152	0.165	0.136	0.151	0.136	0.150	0.136	0.139	0.140	-0.011
8		-0.004	-0.008	-0.011	-0.008	-0.005	-0.002	0.001	-0.005	-0.003	-0.003

Fig. SI-5 | Data analysis of the H-CMZI-A device at 730 nm. a) CG Model of the H-CMZI model, showing top (1) and bottom (2) arms and segment groups 1-8. Each segment can be driven with a positive or negative voltage. b) Raw and normalized power levels and the derived phase shift per segment from sweeping the cumulative phase shift. c) Raw and normalized power levels and the derived phase shift of the 'One-Hot' test, where we activate one segment at a time. d) Processed data grouped by segments of equal size. We ignore values near 0 or pi as the phase derivation is unstable there, and we flip the sign on devices that we expect to produce negative phase shifts (Top M2, Bottom M3)

This data from H-CMZI A is shown in Fig. SI-5. We find that the mean phase shift measured is consistent for both the cumulative phase sweep and the one-hot test, signifying that the device's segments can produce a consistent phase shift independently. We also find the inner-most segment (group 8) does not produce much of a phase shift at all, and the outer-most segment produces a smaller phase shift of 0.074 radians. This is likely because these segments cover less of the waveguide, and impart less of a path length or strain shift when actuated. We find that most segments give a phase shift of approx. 0.11 radians, and the largest phase shift (0.15 radians) comes from Segment Group 7. We see similar results on H-CMZI B, although as this is a larger device we find a maximum phase shift of 0.19 and an average phase shift of 0.12 radians.

SI-7. MZI Modeling and Fitting to Experimental Data

To show the full range of capabilities of our error corrected MZI configuration, we fit the measured data of our triple beamsplitter MZI to a model which accounts for beamsplitter errors α, β, γ, which represent the deviation from a beamsplitting ratio of 0.5, the static phase shift in

the MZI arms φ_0, θ_0. , and the approximate phase shift per segment $\delta\varphi$, $\delta\theta$. These parameters model the behavior of a lossless mach zehnder interferometer with beamsplitting errors due to fabrication intolerances with the linear equations for a Mach Zehnder Interferometer with imperfect beamsplitters[3,4]:

$$\begin{bmatrix} \cos(\pi/4+\gamma) & j\sin(\pi/4+\gamma) \\ j\sin(\pi/4+\gamma) & \cos(\pi/4+\gamma) \end{bmatrix} \begin{bmatrix} e^{j(\theta+\theta_0)} & 0 \\ 0 & 1 \end{bmatrix} \begin{bmatrix} \cos(\pi/4+\beta) & j\sin(\pi/4+\beta) \\ j\sin(\pi/4+\beta) & \cos(\pi/4+\beta) \end{bmatrix} \begin{bmatrix} e^{j(\phi+\phi_0)} & 0 \\ 0 & 1 \end{bmatrix} \begin{bmatrix} \cos(\pi/4+\alpha) & j\sin(\pi/4+\alpha) \\ j\sin(\pi/4+\alpha) & \cos(\pi/4+\alpha) \end{bmatrix}$$

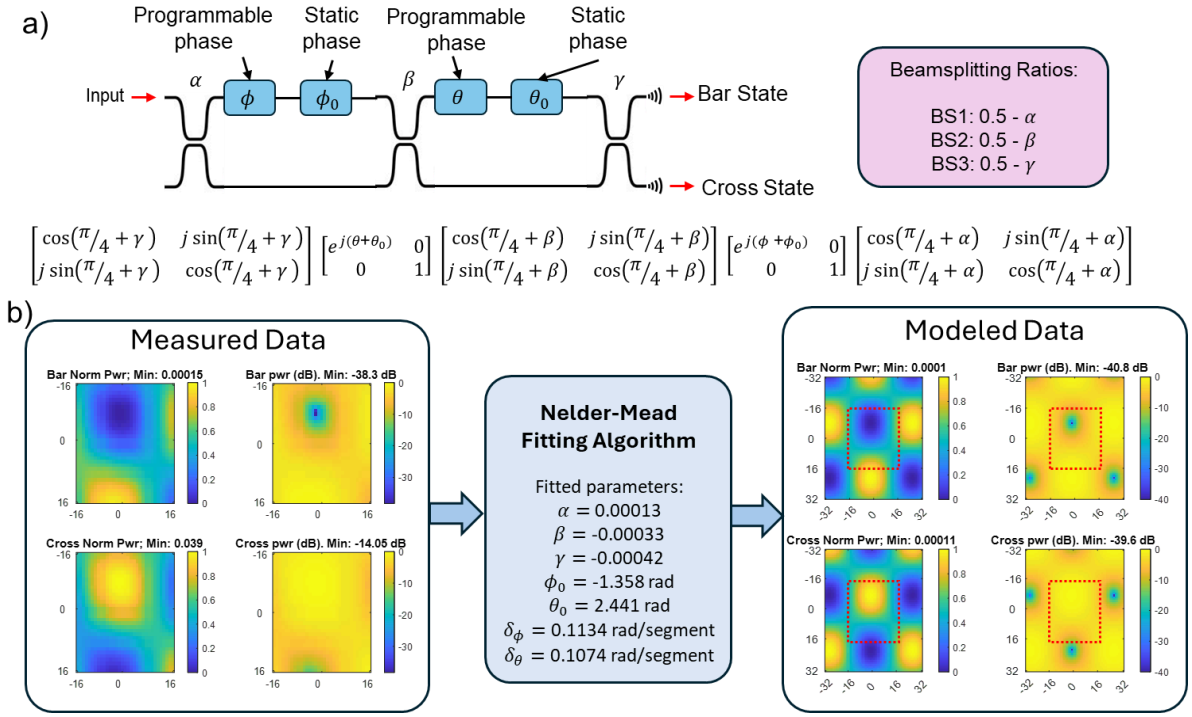

Fig. SI-6 | Modeling the double phase shifter MZI device. a) Block diagram and matrix equations for a lossless double-phase shifter, triple beamsplitter MZI configuration. b) Measured data, extracted parameters, and modeled fit from a Nelder-Meade optimization of the double MZI. We find a high extinction point of >35 dB in the cross state that was just beyond the tuning range of the device

We use a Nelder-Meade algorithm to fit our measured normalized output amplitude data to this model by find parameters of α, β, γ, φ_0, θ_0, $\delta\varphi$, and $\delta\theta$, minimizing the Residual Sum of Square (RSS) value of the measured data compared the model, and plot the modeled range going beyond what we had measured. Fitted parameters are in Fig. SI-4 b and show a modeled actuation range of approximately 0.11 rad/segment. While our model does not account for variable loss in the beamsplitter arms, varying phase shift per segment, or the push-pull nature of our device, it is suitable for comparing to typical MZI behavior and we find an accurate fit (R^2=0.98) which shows a high extinction cross state just outside the experimental tuning range of the device.

SI-8. Ring Resonator Modeling and Analysis

We characterize the ring resonators by first sweeping a tunable laser and observing dips on resonance, from which we fit a Lorentzian curve and extract the ring resonator's Free Spectral Range (FSR), Full Width Half Maximum (FWHM), and Quality Factor. To show piezo-optomechanical detuning of the rings, we set our tunable laser to a fixed wavelength on the amplitude curve halfway between maximum and minimum transmission, either slightly above or slightly below the resonance. We then drive the digital backplane with a target configuration, observe the change in amplitude, and map this amplitude to a detuning frequency shift f based on the amplitude change of our wavelength sweep and fitted Lorentzian curve. We sweep our configuration pattern from -5V on all actuators to +5V on all actuators.

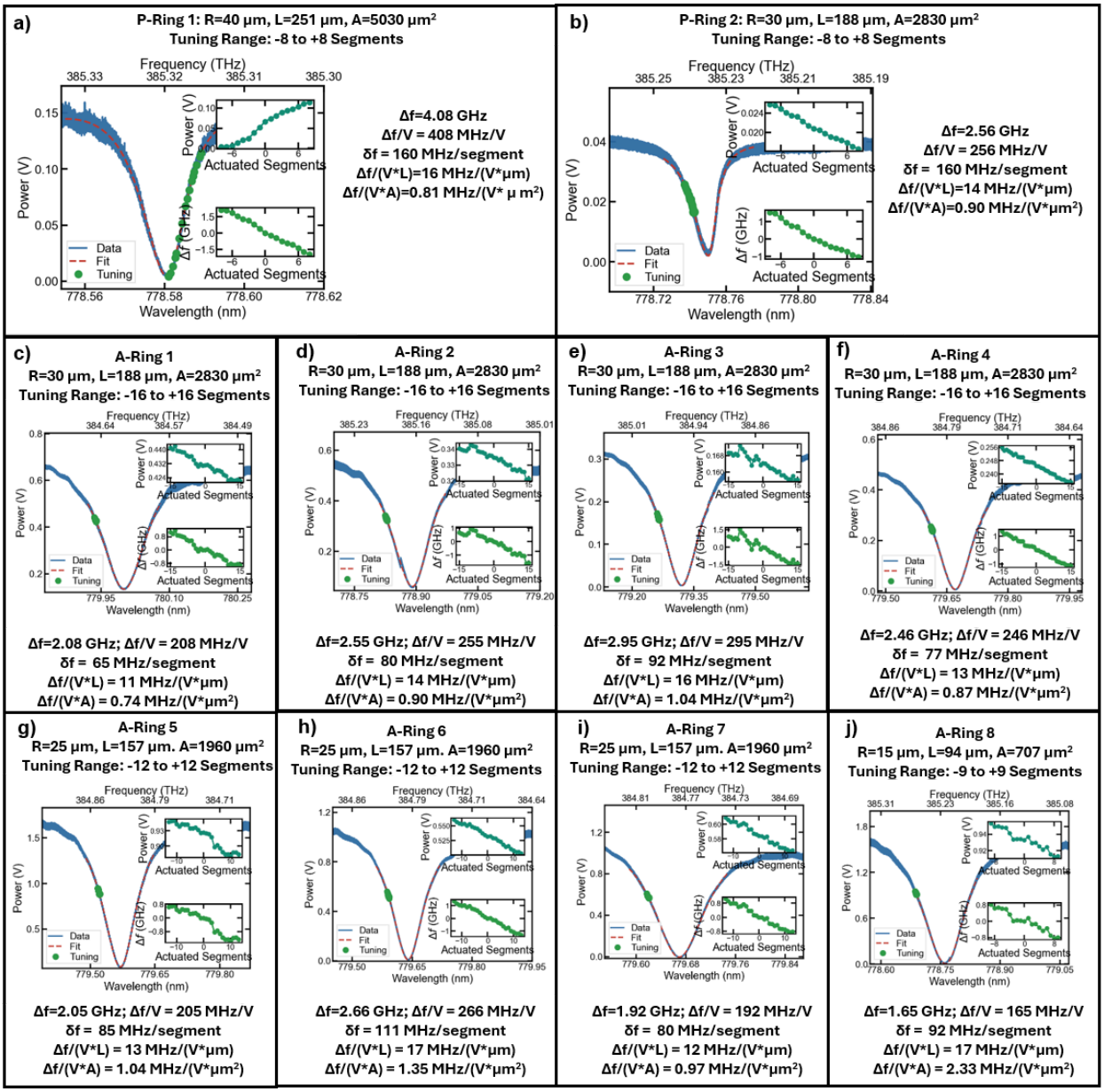

Fig. SI-7 | Ring Resonator Data and Analysis. a-j) Analysis of the 10 ring resonators characterized in Table 2, along with device parameters and extracted detuning, as well as detuning per volt, detuning per segment, detuning per volt-length, and detuning per volt-area.

From this data and analysis, we then extract the total observed tuning Δf over the entire range, the tuning per volt across all segments $\Delta f/V$ (calculated as $\Delta f/10\text{V}$ for the range of -5 to +5V), the tuning per segment δf (calculated as $\Delta f/(2N)$, where N is the number of discrete segments that can be positively or negatively actuated), the length-adjusted tuning per volt $\Delta f/(V\times\mu m)$, and the area-adjusted tuning per volt $\Delta f/(V\times\mu m^2)$. These show how it is comparable to the prior

work in Stanfield et. al[2] which measured detuning of 200 MHz/V on non-undercut 40.8 um rings, and 480 MHz/V on undercut 40.8 μm rings.

Supplementary References

1. Dong, M. *et al.* High-speed programmable photonic circuits in a cryogenically compatible, visible–near-infrared 200 mm CMOS architecture. *Nat. Photonics* **16**, 59–65 (2022).
2. Stanfield, P. R., Leenheer, A. J., Michael, C. P., Sims, R. & Eichenfield, M. CMOS-compatible, piezo-optomechanically tunable photonics for visible wavelengths and cryogenic temperatures. *Opt. Express* **27**, 28588–28605 (2019).
3. Miller, D. A. B. Perfect optics with imperfect components. *Optica* **2**, 747 (2015).
4. Bandyopadhyay, S., Hamerly, R. & Englund, D. Hardware error correction for programmable photonics. *Optica* **8**, 1247 (2021).